ACSNANO

www.acsnano.org

ARTICLE

Almost Perfect Spin Filtering in Graphene-Based Magnetic Tunnel Junctions

Victor Zatko, Simon M.-M. Dubois,[#] Florian Godel, Marta Galbiati, Julian Peiro, Anke Sander, Cécile Carretero, Aymeric Vecchiola, Sophie Collin, Karim Bouzehouane, Bernard Servet, Frédéric Petroff, Jean-Christophe Charlier, Marie-Blandine Martin, Bruno Dlubak,* and Pierre Seneor*

Cite This: *ACS Nano* 2022, 16, 14007−14016

Read Online

ACCESS | Metrics & More | Article Recommendations

ABSTRACT: We report on large spin-filtering effects in epitaxial graphene-based spin valves, strongly enhanced in our specific multilayer case. Our results were obtained by the effective association of chemical vapor deposited (CVD) multilayer graphene with a high quality epitaxial Ni(111) ferromagnetic spin source. We highlight that the Ni(111) spin source electrode crystallinity and metallic state are preserved and stabilized by multilayer graphene CVD growth. Complete nanometric spin valve junctions are fabricated using a local probe indentation process, and spin properties are extracted from the graphene-protected ferromagnetic electrode through the use of a reference Al_2O_3/Co spin analyzer. Strikingly, spin-transport measurements in these structures give rise to large negative tunnel magneto-resistance TMR = −160%, pointing to a particularly large spin polarization for the Ni(111)/Gr interface $P_{Ni/Gr}$, evaluated up to −98%. We then discuss an emerging physical picture of graphene−ferromagnet systems, sustained both by experimental data and ab initio calculations, intimately combining efficient spin filtering effects arising (i) from the bulk band structure of the graphene layers purifying the extracted spin direction, (ii) from the hybridization effects modulating the amplitude of spin polarized scattering states over the first few graphene layers at the interface, and (iii) from the epitaxial interfacial matching of the graphene layers with the spin-polarized Ni surface selecting well-defined spin polarized channels. Importantly, these main spin selection effects are shown to be either cooperating or competing, explaining why our transport results were not observed before. Overall, this study unveils a path to harness the full potential of low Resitance.Area (RA) graphene interfaces in efficient spin-based devices.

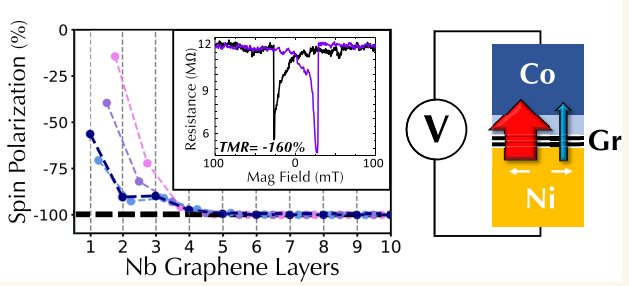

KEYWORDS: *graphene, 2D materials, chemical vapor deposition, spintronics, magnetic tunnel junctions, spin-filtering, magnetoresistance*

INTRODUCTION

Spintronics contributed to the birth of the big data era with highly sensitive hard-drive read-heads allowing dramatic data storage scaling.[1] MRAM, the current spintronics flagship application, promises further increases in efficiency and performance of integrated electronic circuits.[2−4] Furthermore, a unified spin variable is foreseen as a strong post-CMOS asset to merge in-memory processing with stochastic, neuromorphic, and quantum technologies.[5−11] This fuels the quest for further progress in material science toward efficient spin platforms.[12−14] Along this direction, 2D materials have appeared particularly exciting in terms of ultimate atomic interface control and multifunctional heterostructure definition.[15−18] Graphene represents the archetype of all 2D materials and has been put forward for efficient spin transport.[19] It has indeed been demonstrated to efficiently preserve spin information during transport particularly due to its low spin−orbit coupling associated with high mobilities.[20,21] Graphene has furthermore shown promising performances in vertical magnetic tunnel junction (MTJ) spin-valve devices with efficient spin filtering[22−30] as well as stark potential for perpendicular magnetic anisotropy (PMA), spin−orbit torques (SOT), and skyrmion topological spin textures.[31−36]

However, spin transport mechanisms involved in graphene-based 2D-MTJ have just started to be experimentally captured,

Received: April 13, 2022
Accepted: July 14, 2022
Published: September 6, 2022

only recently leading to substantial increases in device performance.[30] Integration issues remain a strong roadblock to fully explore and exploit the potential of graphene for MTJs.[15] Among all the issues which can affect the efficiency of the spin transport in those graphene 2D-MTJs, a crucial role is played by the state of the interface between graphene and the ferromagnetic layer. Indeed, a strong constraint with ferromagnetic spin sources is their immediate oxidation under ambient or oxidative conditions.[37] A typical approach to define 2D-MTJs has been to carry out the micromechanical transfer of the graphene layers on top of the ferromagnetic polarizer. Following this approach, it is highly difficult to prevent degradation of the ferromagnetic layer from the ambient environment. This is a probable reason for the limited amplitude of most TMR spin signals measured in pioneering studies.[15] A scalable approach to the ultraclean interface has been proposed with the direct growth of graphene on top of the ferromagnetic layer using, for instance, a chemical vapor deposition (CVD) growth process.[28] CVD provides large-scale coverage of graphene with growth catalyzed specifically on ferromagnetic metal electrodes, and graphene integrated by CVD is highly efficient to preserve the integrity of ferromagnets surface.[28,36,38] These graphene-protected ferromagnetic electrodes, when integrated in complete MTJs including a reference spin analyzer, have shown a spin polarization of the extracted current ranging from ∼−10%[39] (monolayer graphene on polycrystalline Ni) to ∼−40%[40] (multilayer graphene on polycrystalline Ni). These experiments highlighted a strong increase of the spin polarization with the number of graphene layers. Recently, it has also been shown that growing monolayer graphene on monocrystalline electrodes strongly impacts the spin-polarization, with tailored properties by hybridization emerging from the coupling between graphene and ferromagnets in contact.[30] Nevertheless, overall, high quality integration protocols of graphene on ferromagnets still remain scarce, limiting the exploration of the high potential of this system for spintronics.

In this work, we study the performance of graphene for strong spin filtering by combining a high crystallinity epitaxial ferromagnetic Ni(111) spin source with multilayer graphene in state of the art 2D based magnetic tunnel junctions. We fabricate high-quality heterostructures with a step-by-step approach (supported by XRD, Raman spectroscopy and XPS analyses) checking the preservation and stabilization of the crystalline electrode properties. The resulting electrodes, composed of multilayer graphene grown by CVD on top of crystalline (111) nickel substrates, are then integrated in full MTJ devices. Transport measurements reveal a large spin-filtering effect of the current extracted from the Ni(111)/graphene multilayer electrode with spin polarization evaluated up to a high value $P_{Ni/Gr}$ = −98%, as estimated from the observed large TMR spin signals with TMR > 160% in absolute terms. We then discuss the origin of such a large spin polarization in light of converging experimental data and numerical ab initio analyses, showing the combined action of interfacial and bulk spin filtering effects in the Ni/Gr system.

RESULTS AND DISCUSSION

Figure 1 presents the main fabrication steps of our graphene-based MTJs. First, using a modified Plassys sputtering system, we grow an 80 nm thick Ni(111) electrode on a sapphire (0001) substrate. The growth is made under Ar pressure of 2.5 × 10^{-3} mbar while the substrate is heated at 600 °C by a back

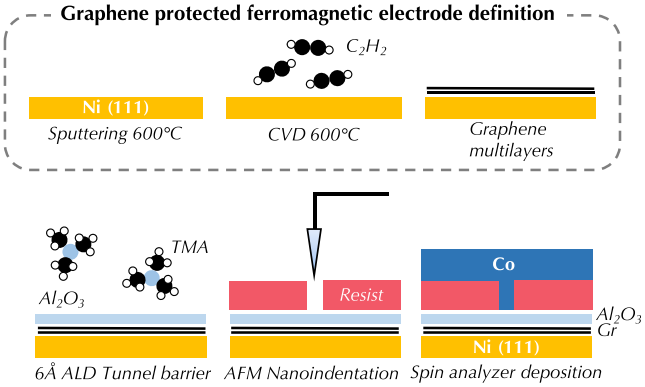

Figure 1. Schematic process flow for the fabrication of epitaxial multilayer graphene-based MTJs. The Ni(111) ferromagnetic spin source is grown by sputtering on sapphire at 600 °C. The graphene multilayer catalytic growth is then carried by exposure to C_2H_2 at 600 °C in an adapted CVD system. The resulting Ni(111)/Gr electrode is then covered with a 6 Å Al_2O_3 tunnel barrier by ALD. A nanojunction is defined in a resist layer by conductive tip AFM nanoindentation. The top Co spin analyzer is then sputtered before the final functional spin valve based on the epitaxial Ni(111)/multilayer graphene electrode is fabricated.

filament. This Ni(111) electrode is then transferred to the CVD chamber for graphene growth. Prior to the graphene growth, we perform a surface preparation under 100 Pa hydrogen atmosphere, annealed at 600 °C (ramped from room-temperature at 300 °C/min) for 15 min. H_2 is removed, and then a precursor gas of C_2H_2 flows into the chamber (1 Pa pressure) while the 600 °C temperature is kept steady to form a multilayer graphene film.[36,41] The graphene growth mechanisms on Ni catalytic substrates have now been well captured[38,41−43] and have been shown to lead to about 5 Bernal stacked layers in our conditions. This particular process gives then rise to a multilayer graphene-covered Ni(111) electrode as analyzed below.

To confirm the crystallinity of the nickel bottom electrode, we perform X-ray diffraction (XRD). Figure 2a shows the XRD spectrum recorded on the initial as-grown 80 nm Ni film grown at 600 °C on sapphire (0001). Clear signatures of Ni(111) and Ni (222) are present and located at 44.53° and 98.63°, respectively. It leads to a lattice parameter of 3.522 Å, close to the bulk one (3.524 Å) for *fcc* Ni. Additional signatures of other orientations are not observed—except for the ones coming from the sapphire substrate—confirming the high quality of the monocrystalline Ni(111) film. To warrant that the high-temperature graphene CVD growth has not impacted the high crystallinity, we carry a further characterization of the XRD signature of the Ni electrode after the CVD step (Figure 2b). It appears that the crystallinity of Ni(111) remains unchanged, with identical peaks relative to Ni being detected. This indicates that the Ni quality is well preserved after the graphene growth. We note that the Ni(111) and Ni(222) peak positions slightly change to 44.63° and 98.79°, respectively, indicating that graphene growth conditions do not impact the Ni film structural properties but might induce a small constraint on the Ni film. This may be related to the fact that the first graphene layer at the interface is coupled to the Ni surface.[30,42] Overall, this shows that the Ni remains in a high-quality monocrystalline state once integrated with the graphene layer. We then investigate the graphene coverage on Ni after our CVD process using Raman spectroscopy and XPS.

https://doi.org/10.1021/acsnano.2c03625
ACS Nano 2022, 16, 14007−14016

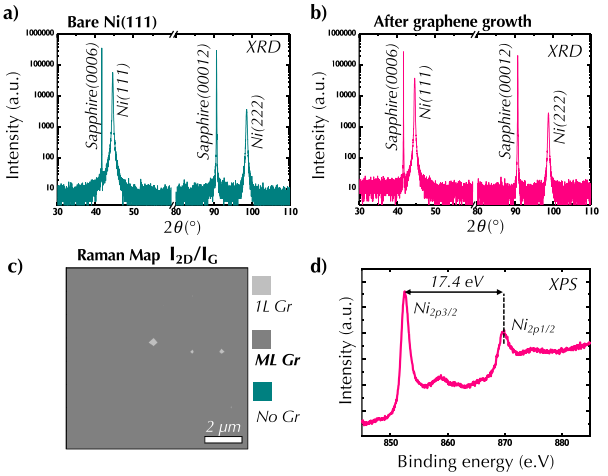

Figure 2. Crystallographic and chemical characterizations of the Ni/Gr electrode. XRD spectra (a) before and (b) after graphene growth on a 80 nm thick Ni(111) electrode. These XRD spectra show that the graphene CVD growth did not change the crystallographic order of the Ni(111) electrode. (c) I_{2D}/I_G Raman map of the multilayer graphene on Ni(111). This characterization shows a homogeneously covered Ni surface with multilayer graphene. (d) XPS study on the same Ni(111) film passivated by graphene shows a metallic Ni surface, demonstrating both the homogeneity of the graphene coverage and its ability to preserve the chemical state of the Ni surface. Overall, these measurements reveal a well-defined Ni/multilayer graphene spin source by our CVD approach.

Figure 2c shows the Raman map of the graphene 2D peak intensity (I_{2D})—normalized by the graphene G peak intensity (I_G)—recorded on a typical 10 × 10 μm^2 Ni(111)/Gr area with discrete steps of 0.5 μm. The I_{2D}/I_G ratio relates to the number of graphene layers surveyed.[44] The Raman map clearly shows the full coverage of Ni(111), with multilayer graphene (MLGr) covering 99.5% of the area as indicated by the I_{2D}/I_G ratio staying below 1 (dark gray), with no holes observed in the film. The chemical state of the graphene-covered Ni surface is also analyzed by XPS. Figure 2d shows the XPS spectrum recorded on Ni(111) substrates after graphene growth and air exposure. Ni $2p_{3/2}$ and Ni $2p_{1/2}$ peaks are separated by an energy of 17.4 eV, which is characteristic of a Ni metallic layer. Furthermore, the global shape of the Ni 2p spectrum and the absence of a peak at 853 eV confirm the full metallic state of the nickel surface.[45] This XPS study highlights the perfect passivation of Ni by our graphene overlayer, corroborating a complete coverage.

In order to explore the spin properties of the multilayer graphene covered Ni(111) electrode, we further integrate it in a full spin valve structure. We make use of a standard Al_2O_3/Co spin analyzer[28] as the top electrode to study the polarization of the extracted current. The sample is transferred to a specially customized ALD chamber directly integrated into a spintronic material deposition cluster. A high-quality 6 Å thin tunnel barrier of Al_2O_3 using trimethylaluminum (TMA) precursor and ozone delivered at 80 °C following previously optimized experimental ALD conditions developed for high wetting on graphene is grown.[30,40] We then define the nanojunction geometry. We employ a voltage-controlled nanoindentation technique[46] where a thin resist (CSAR) is spin coated and nanocontacts are defined by a local probe indentation based on a conductive-tip AFM setup. The AFM tip approach is controlled in real time through the current measurement between the tip and the sample, allowing us to withdraw the tip once in proximity of the bottom electrode. After chemical cleaning, the nanoindentation approach leads to a nanohole of several tens of nanometers in diameter in the resist with a well-defined flat bottom contact surface. Figure 3a

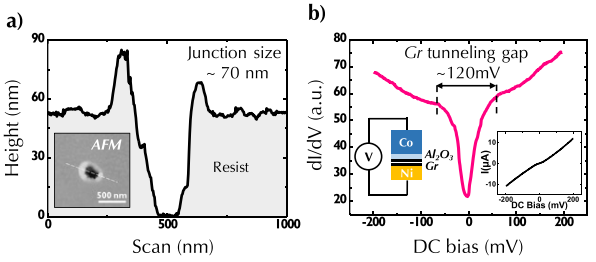

Figure 3. Fabrication of a graphene-based nanojunction. (a) AFM nanoindention profile of the junction after AFM indentation and before Co deposition. The profile corresponds to the dashed line in the inset AFM topography of the junction. Junction size is approximated to 0.004 μm^2. (b) Conductance measurement recorded at 2 K on the graphene-based spin valve (inset: corresponding $I(V)$ on the right, probed junction schematic view on the left). The observed phonon "gap" is a signature of tunneling into the graphene layer and attests to the expected formation of a Ni(111)/Gr/Al_2O_3/Co tunnel junction.

shows the AFM image and section profile of the nanohole above the Ni/Gr/Al_2O_3 heterostructure. A typical width of 70 nm is measured at the bottom of the junction. The top ferromagnetic electrode, 20 nm Co layer capped by Au, is then deposited by sputtering on top of the Al_2O_3. This is an asset of our approach: it indeed allows us to specifically analyze the extracted spin-polarized current with a well-defined reference Al_2O_3/Co tunnel spin analyzer. After shadow masking the junctions with conductive epoxy droplets, a final step of ion beam etching leads to the definition of the complete MTJ structure (schematics shown in Figure 3b inset).

We next characterize the electronic transport behavior and measure at 2 K the voltage dependence of the Gr-based spin valve nanojunction. Figure 3b shows the conductance measurement with respect to the applied bias. The observed conductance response confirms the tunnel transport through the junction with a central dip related to the injection of carriers into graphene with a typical width of 120 mV.[28,47,48] From the junction area we can extract the R.A product of the junction. It ranges from 10^2 to 10^4 Ohm·μm^2 and corresponds to the previous report on 6 Å alumina ALD-based graphene MTJs.[40] These initial transport characterizations confirm the high quality of the spin analyzer that we define using ALD grown tunnel barriers.

Following these initial material validations, we perform magneto-transport measurements to evaluate spin properties of our epitaxial multilayer graphene-based MTJs. Figure 4a shows the typical tunnel magneto resistance (TMR) signal measured at 2 K with an applied DC bias of −5 mV. The parallel magnetic state is measured at 12 MΩ of resistance, which dramatically falls to 4.6 MΩ when the antiparallel state is reached at 27 mT. In order to compare with reported TMR amplitudes, the tunnel magnetoresistance (TMR) in our experiments is defined by $(R_P - R_{AP})/R_{AP}$ for negative TMR, where R_P (R_{AP}) is the resistance in the parallel (antiparallel) state. This corresponds to a TMR spin signal

https://doi.org/10.1021/acsnano.2c03625
ACS Nano 2022, 16, 14007−14016

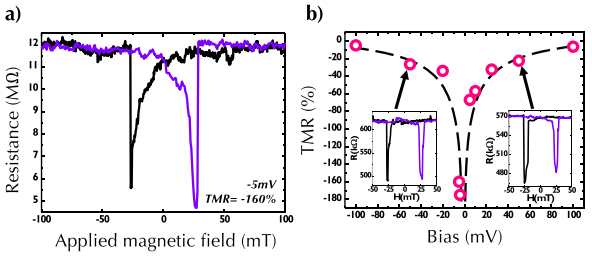

Figure 4. Spin-transport characterizations in the multilayer Ni(111)/MLGr based spin valve making use of the top Al_2O_3/Co spin analyzer. (a) Magneto-resistance signal measured at 2 K and under −5 mV DC bias in the nanojunction. The negative TMR observed of −160% comes from the efficient spin filtering effect occurring at the Ni(111)/Gr interface and leads to an extracted large negative spin polarization up to $P_{Ni/Gr}$ = −98%. (b) TMR dependency with respect to the DC bias applied in the junction with pink circles being experimental TMR measured at different biases (black dashed line is a guide-to-the-eye). We observe only a simple monotonous dependence of the TMR spin signal with bias, classically ascribed to FM magnons (see refs 52 and 53). Inset: two TMR measured at + and −50 mV.

value equal to −160% for a bias of −5 mV. Extending this magneto-transport measurement to other DC-applied bias (Figure 4b), we observe a progressive decrease of the TMR ratio with respect to the increasing bias reaching ∼−6% at ±100 mV. Interestingly, from the Julliere[49] model and the value of the TMR we can extract the spin polarization of the Ni/Gr electrode given by $P_{Ni/Gr}$ = TMR/[(2 − TMR) $P_{Co/AlOx}$]. We take for our Co/amorphous-alumina interface the best recorded spin polarization of $P_{Co/AlOx}$ = +45%.[50,51] The spin polarization for the bottom Ni(111)/Gr electrode then reaches $P_{Ni/Gr}$ = −98%, highlighting the efficient spin filtering effect occurring at the Ni(111)/MLGr interface.

To understand the origin of this effect, this result is compared to previous studies on similar spin valves structures encompassing a graphene layer using the CVD integration approach (see Table 1). Previously, it has been shown that going from monolayer to multilayer graphene on polycrystalline Ni led to a drastic increase of the extracted spin polarization, corresponding to a 5× increase of the TMR.[40,39,15] This has been ascribed[15] to the efficient filtering of majority spins by multilayer graphene due to K point selection at the Fermi surface of nickel, as described in ref 26. Independently, for monolayer graphene, it has been shown that going from polycrystalline to monocrystalline Ni(111) also led to an increase of the interfacial spin-filtering corresponding to a 2× increase of the measured TMR. This allowed us to reach toward the ideal epitaxial situation for spin selection of ref 26 and leveraging from hybridization effects.[30] In the presented spin valve heterostructure we engineered a system combining a multilayer graphene spin-filtering membrane with a monocrystalline Ni(111) spin source, capitalizing on what appear to be complementary conditions to increase the spin selectivity of the Ni/Gr interface: Ni epitaxy for proper interfacial hybridization with pure Ni(111) spin channels and additional graphene layer stacking for increased spin filtering. In this way, we reached an increase of the spin signal by 20× over the initial study of monolayer graphene on polycrystalline nickel.

Table 1. Measured TMR Spin Signals and Extracted Spin Polarizations from Various Ni/Gr Interfaces Defined by the CVD Approach and Making Use of an ALD Al_2O_3/Co Spin Analyzer[a]

	monolayer graphene	multilayer graphene
polycrystalline Ni	TMR = −5.8%	TMR = −31%
	P = −9.8%	P = −42%
	ref 39	ref 40
monocrystalline Ni(111)	TMR = −12%	TMR = −160%
	P = −20%	P = −98%
	ref 30	(this work)

[a]The devices present different spin signals depending on their different crystallinity and graphene layer stacks. This analysis highlights the importance of matching graphene with a crystalline spin source to select efficiently one spin direction and to maximize the filtering effect by increasing the number of stacked graphene layers (this work).

The robustness of spin-filtering by crystal-momentum selection and the instrumental role of interfacial hybridization are further confirmed by first-principles calculations. Here, we consider transport across the Ni(111)/graphene interface within the framework of nonequilibrium Green's function formalism. The computational device setup is depicted in Figure 5a. It is built up from 12 atomic planes of nickel along the fcc ⟨111⟩ direction and 14 planes of multilayer graphene in an AB-stacking sequence (i.e., graphite). The semi-infinite nature of nickel and AB-stacked MLGr perpendicular to the interface (i.e., the direction of transport) is accounted for by introducing contact self-energies ($\Sigma_{Ni/G}$) on the last three Ni atomic planes and the last two graphene layers. Periodic boundary conditions are considered in directions perpendicular to transport.

We consider first the epitaxial stacking of the MLGr on the ferromagnet. This is the ground-state configuration.[26,54,55] From the computed Green's functions, we visualize the modulation of the electronic dispersion across the junction (see Figure 5b,c), and we compute the transmission coefficients (see Figure 6a). Away from the interface, one recovers the electronic structure of bulk Ni and graphite. On the one hand, the low energy density of states of Ni is dominated by the d-electron bands of minority spin (Figure 5b). On the other hand, graphite is characterized by a vanishing energy gap and finite density of state at the Fermi level around the high-symmetry K-points (Figure 5c). At the interface, the electronic structure is ruled by proximity-induced hybridization (including charge transfer and exchange as discussed in ref 56). In the ground-state epitaxial configuration, the first carbon plane strongly hybridizes to Ni(111) with a resulting Ni−C interlayer distance of ∼2.2 Å. The computed transmission coefficients are depicted in Figure 6a. The filtering of majority spin carriers by crystal momentum selection is clearly evidenced at low energy. Large metallic transmission coefficients are reported around the K-point for minority spin carriers, while a tunneling transport gap of ∼2 eV prevents the propagation of the majority of spin carriers. To further illustrate this behavior, we analyze the density of scattering states (DOSS) originating in nickel. The layer-resolved DOSS is evaluated as a partial trace of the spectral function formed from left-incoming (i.e., nickel to MLGr) flux-normalized scattering states only.[57] The strongly evanescent character of the majority spin carriers is easily deduced from the fast exponential decay of the layer-resolved DOSS depicted in Figure 7a. Oppositely, the formation of propagating spin-minority eigenchannels associated with large transmission

https://doi.org/10.1021/acsnano.2c03625
ACS Nano 2022, 16, 14007−14016

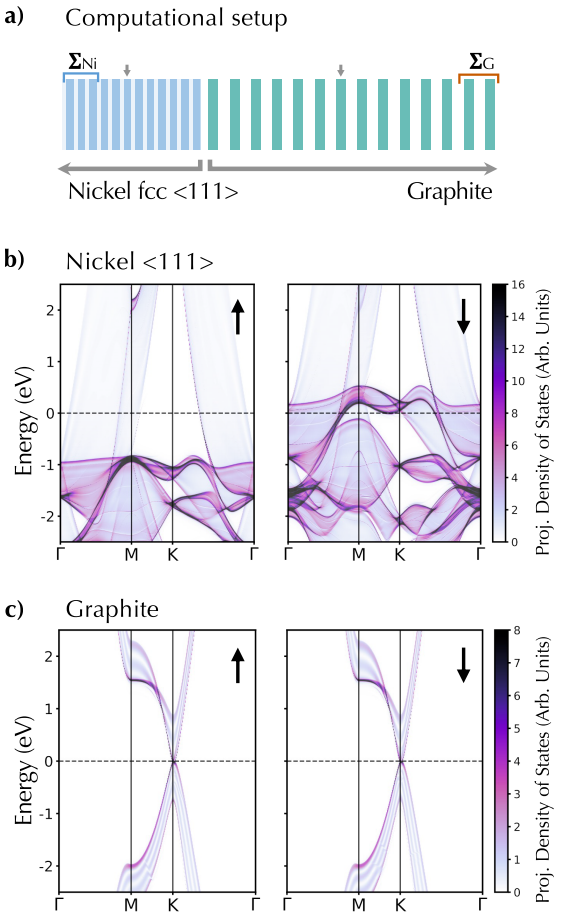

Figure 5. (a) Schematic representation of the computational setup used for the evaluation of the Green's function of the Ni(111)/MLGr interface. The device is composed of 12 atomic layers of Ni along the fcc ⟨111⟩ direction and 14 layers of AB-stacked graphene. Periodic boundary conditions are imposed in the directions perpendicular to transport. Contact self-energies (Σ_{Ni} and Σ_G) are introduced at the extremities to account for the semi-infinite nature of nickel and MLGr. (b,c) Electronic band structures of Ni and MLGr away from the interface. Electronic dispersion along the conventional high symmetry k-path in the plane parallel to the interface, computed from Green's function projected on the atomic layers indicated by an arrow in (a). Left and right panels correspond, respectively, to the majority and minority spin carriers.

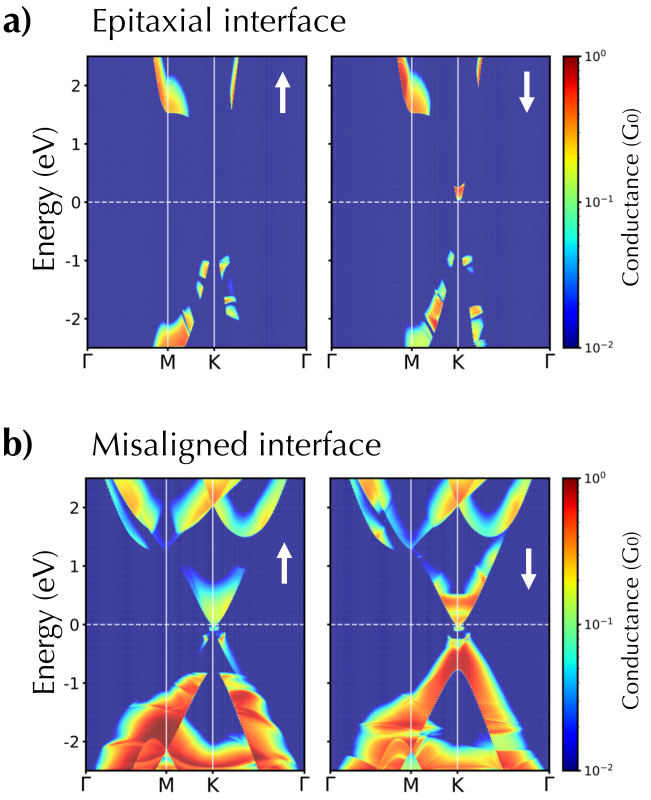

Figure 6. Electronic transmission across (a) the epitaxial and (b) the misaligned Ni/MLGr interfaces. Transmission coefficients are depicted in units of the quantum of conductance (G_0) along the conventional high symmetry k-path in the plane parallel to the interface. Left and right panels correspond respectively to majority and minority spin carriers. It is observed that the epitaxial case provides a highly asymmetrical spin-dependent transport channel, while a more balanced (but hence less spin polarized) spin transport is achieved in the misaligned case.

coefficients around the K-point manifests itself by fixing a limit to the attenuation of the minority spin DOSS. As a result, after a few layers, the difference in majority and minority transmission is already more than 1 order of magnitude and reaches 9 orders of magnitude after 10 layers. As such, the DOSS spin-polarization quickly builds up as the carriers penetrate into the MLGr (see Figure 7b). Owing to the many evanescent scattering states characterized by short decay length, the spin-polarization shows large variations on the first few graphene layers where details of hybridization play a major role in shaping the electronic landscape. Beyond the fifth graphene plane, the spin-minority propagating states dominate the DOSS and the computed spin polarization approaches −100%. This is in clear agreement with the −98% high spin-polarization deduced from our experiments.

One may question how robust this observation is and why it has not been reported before. Questions on the robustness of the spin filtering in graphene were already raised in earlier theoretical works,[26] and proximity-induced exchange on graphene has been further discussed in refs 15, 30, 56, and 58. On the one hand, the graphene layer grown epitaxially on nickel has been shown to strongly hybridize, asymmetrically altering its characteristic linear electronic dispersion at low energy (K-points) and leading to strong spin-splitting.[15,30] On the other hand, spin-splitting and charge transfer with an adjacent ferromagnetic surface have also been reported to modulate the spin-transport behavior of the nonepitaxial, weakly bound graphene/FM interface.[56] In fact, the spin-dependent properties of proximitized graphene are expected to be strongly dependent on the graphene/ferromagnet distance and orientation.[30] We have numerically tested the robustness of band spin filtering with respect to these two factors. Starting with the ground-state epitaxial configuration, the graphene/Ni separation has been varied while keeping other parameters constant (i.e., without further relaxation of internal coordinates). In this way, the epitaxial character of the interface was preserved while the strength of the hybridization between graphene and Ni was artificially modulated. This serves to highlight the role of hybridization and charge transfer in the epitaxial configuration. The strong impact of proximity effects

https://doi.org/10.1021/acsnano.2c03625
ACS Nano 2022, 16, 14007−14016

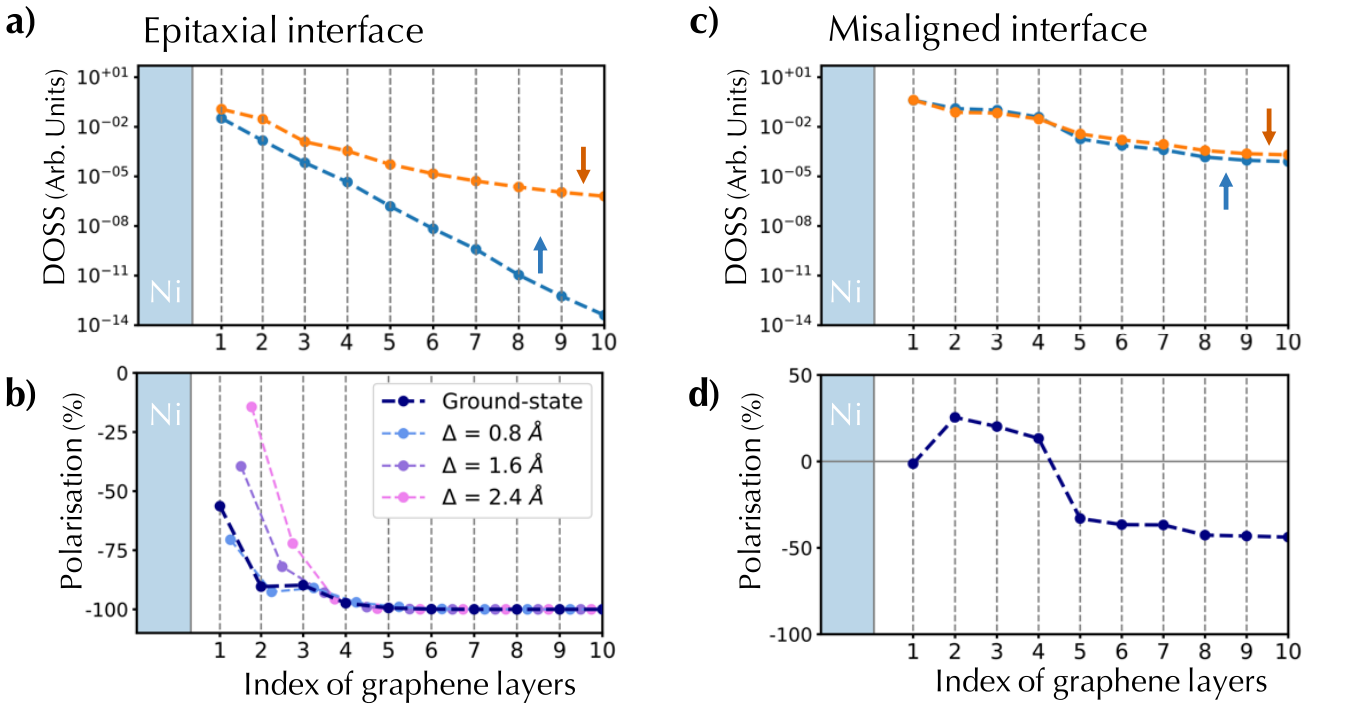

Figure 7. Layer resolved density of scattering states evaluated as a partial trace of the spectral function built out of the Ni-incoming scattering states for both (a) the epitaxial and (c) the misaligned Ni/AB-stacked graphene interfaces. Blue and orange dots correspond respectively to spin majority and spin minority carriers. (b,d) Relative spin-polarization of the density of scattering states. The spin-polarization of the relaxed epitaxial and misaligned configurations are depicted in navy blue. In panel (b), the extra curves correspond to the spin-polarization computed when modulating the Ni/AB-stacked graphene separation by increments of 0.8 Å. Overall, the epitaxial conditions, by matching a highly asymmetric spin transport configuration as shown in Figure 6, fulfills strong K-point graphene spin filtering.

on the spin-polarization of the first four graphene layers is highlighted in Figure 7b. Spin-polarizations ranging from −14% up to −70% are reported for the first graphene layer. This corroborates the spin polarization of −20% previously deduced experimentally for monolayer graphene on monocrystalline Ni(111).[30] Further away from the interface, the band-filtering mechanism dominates, resulting in large polarization, as expected independently of the interfacial hybridization strength. The situation is quite different when the graphitic stack is misaligned with the nickel surface. An example of such an effect is given in Figures 6 and 7 comparing the epitaxial and misaligned cases. The misaligned case is obtained by rotating the stack by 21.79° with respect to nickel, allowing such a configuration to be obtained without introducing additional strain at the interface.[30] After relaxation of the ionic degrees of freedom at the interface, we obtain a Ni/graphene separation of ∼3.04 Å, corresponding to a weakly interacting vdW interface between graphene and the ferromagnet. In this configuration, graphene's linear spectrum is preserved but the absence of precise lattice matching and alignment between graphene and the ferromagnet proscribes strict spin momentum selection mechanisms. Indeed, the crystal momentum selection operated by the graphitic band structure around the K and K′ high-symmetry point samples finite densities of states on the Ni(111) Fermi surface for both the majority and minority spin carriers. As a result, this time, significant transmission coefficients are reported for both spin channels around the Fermi level (see Figure 6b). Accordingly, the layer-resolved DOSS does not show the exponential decay of the majority spin carriers as in the epitaxial case, confirming the formation of propagating channels for both majority and minority spin carriers (see Figure 7c). In this situation, the DOSS spin polarization on the first few graphene layers is determined by the doping of graphene and the exchange induced by the adjacent ferromagnet. Deep into the AB-stacked graphene the DOSS spin polarization saturates. For the particular misaligned geometry considered in our calculation, we report a saturation value ∼−40% (see Figure 7d) in very good agreement with the experimental evidence of −42% for nonepitaxial spin-valve structures encompassing multilayer graphene.[40] Interestingly, as shown in Figure 7d, in this case the proximity effects may give rise to a positive spin polarization of the propagating states on the first few layers of graphene, opposite to the effect K-point band structure spin filtering. Overall, this theoretical analysis highlights that the relative alignment of the graphene and nickel interfaces and their coupling are the main drivers to reach the ideal conditions of graphene K-point filtering at the interface. This corroborates the observed experimental trend (see Table 1).

CONCLUSION

In conclusion, we developed an approach based on the direct integration of multilayer graphene grown by CVD on Ni(111) surfaces. This unlocks pristine integration of epitaxial graphene/nickel interfaces into functional spin valve devices, preserving the crystallinity of nickel and protecting it from oxidation. A TMR spin signal amplitude of −160% is recorded in the complete graphene based MTJs. This corresponds to a particularly large negative spin polarization of the extracted current evaluated up to −98% and highlights the efficiency of the spin filtering effects arising at the Ni(111)/Gr interface. Our experimental result appears thus as a strong confirmation

https://doi.org/10.1021/acsnano.2c03625
ACS Nano 2022, 16, 14007−14016

of the initial projections drawn for graphene−nickel interfaces.[26,15] Importantly, we unveil the key conditions required to achieve them and explain why it was not observed before. Indeed, a physical picture of spin transport in this system finally emerges from accumulated experiments (this and previous work) and correlated ab initio calculations, revealing the fundamental spin selection mechanisms arising at the interface. Two main class of effects, (a) "bulk" K-point band structure filtering and (b) interfacial hybridization (including charge transfer and proximity induced spin-splitting), are either cooperating or competing. Ultimately, we identify three key parameters whose cooperation is shown to be fundamental to achieve our result: (i) having a K-point bulk spin filtering mechanism in multilayer graphene selecting minority spins from the nickel surface, (ii) obtaining a tailored interfacial hybridization (depending on the coupling strength) projecting a strong negative (i.e., minority) spin polarization on the first graphene layers (in a "spinterface" way[59]), and (iii) fully satisfying the matching of graphene K-point conduction and hybridized interface with nickel, i.e., Ni(111) epitaxial conditions. As such, in these unique conditions, the minority spin-polarized current is selected at the nickel/graphene-hybridized interface and is further strengthened through the bulk K-point spin selectivity to achieve full spin polarization of the extracted current for the multilayer case. Their respective identification highlights effects that can be cooperative or competitive with perspectives for individual tailoring and exploitation to adjust spin-valve response. Indeed, refs 30 and 60 highlight that the control of the hybridization by proximity effect of the top spin electrode with graphene as well as other 2D materials, away from the conventional Co/Al_2O_3 tunnel spin analyzer used here, is key to engineer large spin polarization by hybridization (ref 30 presents a 6× increase of the spin signal by proximity with Co), and unveils an impressive perspective to reach even larger MR in graphene-based MTJs compared to the presented results. Furthermore, spin selectivity can be adapted further beyond the Dirac band structure of graphene, for instance using the tailorable band-gaps of TMDC 2D semiconductors family leading to a related K-Q spin filtering effect.[61] The association of 2D materials in heterostructures on top of crystalline spin sources, with 2D stack band structure landscape engineering,[16] could thus provide an efficient solution to propose original spin functions in envisioned complex spin-circuits.[3,8,10] Overall, this study is an illustration of the opportunities offered by 2D materials-based interfaces with ferromagnets for spintronics post-CMOS visions.

METHODS

Graphene-Passivated Spin Sources. The Ni layer is formed by magnetron sputtering while the graphene layers are grown by CVD. A 80 nm Ni(111) layer is first epitaxially grown by sputtering on monocrystalline sapphire (0001) in a customized PLASSYS MP-900S system.[30] The growth is carried at 600 °C in an 80 W Ar plasma and at a rate of 1.89A/s. Multilayer graphene is then epitaxially grown by CVD on top of the Ni(111) electrodes in a customized cold-wall JCVD reactor whose base pressure is 5.10^{-7} mbar.[28,36,40,62] The Ni(111) films are heated to 600 °C in a 100 Pa H_2 atmosphere at a rate of 300 °C/min and annealed for 15 min. The H_2 is then removed and the samples are exposed to 1 Pa C_2H_2 atmosphere at 600 °C for 15 min to form the graphene multilayers. Finally, the samples are left to cool in a vacuum.

Nanodevice Fabrication. The Al_2O_3 tunnel barrier is grown using a customized BENEQ atomic layer deposition (ALD) growth system, directly integrated into the spintronic material deposition cluster. Initially, a 60 s ozone absorption step is carried to reach high conformality required for continuous Al_2O_3 tunnel barrier growth.[40] The tunnel barrier growth is then achieved by carrying 6 cycles of trimethylaluminum (TMA) and ozone delivered at 80 °C sequentially, with a growth rate of 1 A per cycle.[30] An insulating CSAR resist layer is then spin-coated on the surface and nanocontacts are defined by an AFM local probe voltage controlled nano-indentation technique.[46] Exposed CSAR nanosurfaces are selectively chemically etched leading to junctions several tens of nanometers in diameter. Sputtering is finally used to deposit gold capped Co spin analyzer through the nanojunctions.[61,30] The devices are then bonded and integrated in a ceramic chip for further electrical characterizations.

First-Principles Calculations. Green's functions and self-energies are evaluated using the vdW-DF functional of Dion et al.[63] with the exchange modified by Klimeš et al.[64] as implemented within the (Trans-)Siesta package.[65−68] Basis sets of numerical atomic orbitals (double-ζ + polarization) are used to expand the electronic eigenstates manifold. Integration in reciprocal space is performed on regular grids characterized by an effective cutoff ≥40 Å. The lattice parameter of nickel and graphite perpendicular to the transport direction has been fixed to 3.522 Å. The remaining lattice parameters have been optimized in periodic bulk conditions, resulting in 6.10 and 6.48 Å for Ni and graphite, respectively. Eventually, the ionic degrees of freedom of the three surface atomic layers of nickel and the two first graphene planes have been optimized up to atomic forces lower than 0.01 eV/Å. Spin−orbit coupling in the multilayer graphene is not expected to impact the results of our analysis. Organic systems including graphene present particularly limited spin−orbit coupling and hyperfine interactions compared to usual semiconductors such as Si and GaAs (as they are mostly formed by light elements and transport is usually carried by π orbitals), with resulting expected long spin lifetimes and corresponding spin diffusion lengths, see illustratively predictions in refs 69 and 70 and the extensive experimental evidence starting with Krinichnyi et al.[71] and even including amorphous organic layers as, for instance, in Shim et al.[72]

AUTHOR INFORMATION

Corresponding Authors

Bruno Dlubak − *Unité Mixte de Physique, CNRS, Thales, Université Paris-Saclay, 91767 Palaiseau, France;* orcid.org/0000-0001-5696-8991; Email: bruno.dlubak@cnrs-thales.fr

Pierre Seneor − *Unité Mixte de Physique, CNRS, Thales, Université Paris-Saclay, 91767 Palaiseau, France;* Email: pierre.seneor@cnrs-thales.fr

Authors

Victor Zatko − *Unité Mixte de Physique, CNRS, Thales, Université Paris-Saclay, 91767 Palaiseau, France;* orcid.org/0000-0002-2475-8866

Simon M.-M. Dubois − *Institute of Condensed Matter and Nanosciences (IMCN), Université Catholique de Louvain (UCLouvain), B-1348 Louvain-la-Neuve, Belgium*

Florian Godel − *Unité Mixte de Physique, CNRS, Thales, Université Paris-Saclay, 91767 Palaiseau, France;* orcid.org/0000-0003-1741-2741

Marta Galbiati − *Unité Mixte de Physique, CNRS, Thales, Université Paris-Saclay, 91767 Palaiseau, France*

Julian Peiro − *Unité Mixte de Physique, CNRS, Thales, Université Paris-Saclay, 91767 Palaiseau, France*

Anke Sander − *Unité Mixte de Physique, CNRS, Thales, Université Paris-Saclay, 91767 Palaiseau, France*

Cécile Carretero − *Unité Mixte de Physique, CNRS, Thales, Université Paris-Saclay, 91767 Palaiseau, France*

https://doi.org/10.1021/acsnano.2c03625
ACS Nano 2022, 16, 14007−14016

Aymeric Vecchiola − *Unité Mixte de Physique, CNRS, Thales, Université Paris-Saclay, 91767 Palaiseau, France*
Sophie Collin − *Unité Mixte de Physique, CNRS, Thales, Université Paris-Saclay, 91767 Palaiseau, France*
Karim Bouzehouane − *Unité Mixte de Physique, CNRS, Thales, Université Paris-Saclay, 91767 Palaiseau, France*
Bernard Servet − *Thales Research and Technology, 91767 Palaiseau, France*
Frédéric Petroff − *Unité Mixte de Physique, CNRS, Thales, Université Paris-Saclay, 91767 Palaiseau, France*
Jean-Christophe Charlier − *Institute of Condensed Matter and Nanosciences (IMCN), Université Catholique de Louvain (UCLouvain), B-1348 Louvain-la-Neuve, Belgium*
Marie-Blandine Martin − *Unité Mixte de Physique, CNRS, Thales, Université Paris-Saclay, 91767 Palaiseau, France*

Complete contact information is available at: https://pubs.acs.org/10.1021/acsnano.2c03625

Author Contributions

#S.M.-M.D.: first author for theoretical part.

Notes

The authors declare no competing financial interest.

ACKNOWLEDGMENTS

This project has received funding from the European Union's H2020 Future and Emerging Technologies Graphene Flagship (Grant Core3 No. 881603). This research is supported by a public grant overseen by the French National Research Agency (ANR) as part of the "Investissements d'Avenir" program Labex NanoSaclay (ANR-10-LABX-0035), as well as grants MIXES (ANR-19-CE09-0028) and STEM2D (ANR-19-CE24-0015), by the F.R.S.-FNRS through the research project MOIRÉ (No. T.029.22F), by the Fédération Wallonie-Bruxelles through ARC Grants (Nos. 16/21-077 and 21/26-116), by the EOS project CONNECT (No. 40007563), and by the Flag-ERA JTC 2019 project entitled "SOGraphMEM" (ANR-19-GRFI-0001-07, R.8012.19). Computational resources were provided by the supercomputing facilities of the Université Catholique de Louvain (CISM) and the Consortium des Équipements de Calcul Intensif en Fédération Wallonie Bruxelles (CÉCI) funded by the Fonds de la Recherche Scientifique de Belgique (F.R.S.-FNRS) under the convention No. 2.5020.11.

REFERENCES

(1) Chappert, C.; Fert, A.; Van Dau, F. N. The Emergence of Spin Electronics in Data Storage. *Nat. Mater.* **2007**, *6* (11), 813−823.
(2) Khvalkovskiy, A. V.; Apalkov, D.; Watts, S.; Chepulskii, R.; Beach, R. S.; Ong, A.; Tang, X.; Driskill-Smith, A.; Butler, W. H.; Visscher, P. B.; Lottis, D.; Chen, E.; Nikitin, V.; Krounbi, M. Basic Principles of STT-MRAM Cell Operation in Memory Arrays. *J. Phys. D: Appl. Phys.* **2013**, *46* (7), 074001.
(3) Dieny, B.; Prejbeanu, I. L.; Garello, K.; Gambardella, P.; Freitas, P.; Lehndorff, R.; Raberg, W.; Ebels, U.; Demokritov, S. O.; Akerman, J.; Deac, A.; Pirro, P.; Adelmann, C.; Anane, A.; Chumak, A. v.; Hirohata, A.; Mangin, S.; Valenzuela, S. O.; Onbaşlı, M. C.; d'Aquino, M.; Prenat, G.; Finocchio, G.; Lopez-Diaz, L.; Chantrell, R.; Chubykalo-Fesenko, O.; Bortolotti, P. Opportunities and Challenges for Spintronics in the Microelectronics Industry. *Nature Electronics* **2020**, *3* (8), 446−459.
(4) Zhu, L.; Bamberg, L.; Agnesina, A.; Catthoor, F.; Milojevic, D.; Komalan, M.; Ryckaert, J.; Garcia-Ortiz, A.; Lim, S. K. Heterogeneous 3D Integration for a RISC-V System with STT-MRAM. *IEEE Computer Architecture Letters* **2020**, *19* (1), 51−54.
(5) Behin-Aein, B.; Datta, D.; Salahuddin, S.; Datta, S. Proposal for an All-Spin Logic Device with Built-in Memory. *Nat. Nanotechnol* **2010**, *5* (4), 266−270.
(6) Awschalom, D. D.; Bassett, L. C.; Dzurak, A. S.; Hu, E. L.; Petta, J. R. Quantum Spintronics: Engineering and Manipulating Atom-like Spins in Semiconductors. *Science (1979)* **2013**, *339* (6124), 1174−1179.
(7) Mizrahi, A.; Hirtzlin, T.; Fukushima, A.; Kubota, H.; Yuasa, S.; Grollier, J.; Querlioz, D. Neural-like Computing with Populations of Superparamagnetic Basis Functions. *Nat. Commun.* **2018**, *9* (1), 1533.
(8) Manipatruni, S.; Nikonov, D. E.; Lin, C. C.; Gosavi, T. A.; Liu, H.; Prasad, B.; Huang, Y. L.; Bonturim, E.; Ramesh, R.; Young, I. A. Scalable Energy-Efficient Magnetoelectric Spin−Orbit Logic. *Nature* **2019**, *565* (7737), 35−42.
(9) Borders, W. A.; Pervaiz, A. Z.; Fukami, S.; Camsari, K. Y.; Ohno, H.; Datta, S. Integer Factorization Using Stochastic Magnetic Tunnel Junctions. *Nature* **2019**, *573* (7774), 390−393.
(10) Grollier, J.; Querlioz, D.; Camsari, K. Y.; Everschor-Sitte, K.; Fukami, S.; Stiles, M. D. Neuromorphic Spintronics. *Nature Electronics* **2020**, *3* (7), 360−370.
(11) Jung, S.; Lee, H.; Myung, S.; Kim, H.; Yoon, S. K.; Kwon, S.-W.; Ju, Y.; Kim, M.; Yi, W.; Han, S.; Kwon, B.; Seo, B.; Lee, K.; Koh, G.-H.; Lee, K.; Song, Y.; Choi, C.; Ham, D.; Kim, S. J. A Crossbar Array of Magnetoresistive Memory Devices for In-Memory Computing. *Nature* **2022**, *601* (7892), 211−216.
(12) Felser, C.; Fecher, G. H.; Balke, B. Spintronics: A Challenge for Materials Science and Solid-State Chemistry. *Angew. Chem., Int. Ed.* **2007**, *46* (5), 668−699.
(13) Lin, X.; Yang, W.; Wang, K. L.; Zhao, W. Two-Dimensional Spintronics for Low-Power Electronics. *Nature Electronics* **2019**, *2* (7), 274−283.
(14) Giustino, F.; Lee, J. H.; Trier, F.; Bibes, M.; Winter, S. M.; Valentí, R.; Son, Y. W.; Taillefer, L.; Heil, C.; Figueroa, A. I.; Plaçais, B.; Wu, Q. S.; Yazyev, O. v.; Bakkers, E. P. A. M.; Nygård, J.; Forn-Díaz, P.; de Franceschi, S.; McIver, J. W.; Foa Torres, L. E. F.; Low, T.; Kumar, A.; Galceran, R.; Valenzuela, S. O.; Costache, M. v.; Manchon, A.; Kim, E. A.; Schleder, G. R.; Fazzio, A.; Roche, S. The 2021 Quantum Materials Roadmap. *Journal of Physics: Materials* **2021**, *3* (4), 042006.
(15) Piquemal-Banci, M.; Galceran, R.; Martin, M.-B.; Godel, F.; Anane, A.; Petroff, F.; Dlubak, B.; Seneor, P. 2D-MTJs: Introducing 2D Materials in Magnetic Tunnel Junctions. *J. Phys. D: Appl. Phys.* **2017**, *50* (20), 203002.
(16) Zatko, V.; Dubois, S. M.-M.; Godel, F.; Carrétéro, C.; Sander, A.; Collin, S.; Galbiati, M.; Peiro, J.; Panciera, F.; Patriarche, G.; Brus, P.; Servet, B.; Charlier, J.-C.; Martin, M.-B.; Dlubak, B.; Seneor, P. Band-Gap Landscape Engineering in Large-Scale 2D Semiconductor van Der Waals Heterostructures. *ACS Nano* **2021**, *15* (4), 7279−7289.
(17) Sierra, J. F.; Fabian, J.; Kawakami, R. K.; Roche, S.; Valenzuela, S. O. Van Der Waals Heterostructures for Spintronics and Opto-Spintronics. *Nat. Nanotechnol.* **2021**, *16* (8), 856−868.
(18) Husain, S.; Gupta, R.; Kumar, A.; Kumar, P.; Behera, N.; Brucas, R.; Chaudhary, S.; Svedlindh, P. Emergence of Spin−Orbit Torques in 2D Transition Metal Dichalcogenides: A Status Update. *Applied Physics Reviews* **2020**, *7* (4), 041312.
(19) Roche, S.; Åkerman, J.; Beschoten, B.; Charlier, J.-C.; Chshiev, M.; Dash, S. P.; Dlubak, B.; Fabian, J.; Fert, A.; Guimarães, M.; Guinea, F.; Grigorieva, I.; Schönenberger, C.; Seneor, P.; Stampfer, C.; Valenzuela, S. O.; Waintal, X.; van Wees, B. Graphene Spintronics: The European Flagship Perspective. *2D Materials* **2015**, *2* (3), 30202.
(20) Huertas-Hernando, D.; Guinea, F.; Brataas, A. Spin-Orbit Coupling in Curved Graphene, Fullerenes, Nanotubes, and Nanotube Caps. *Phys. Rev. B* **2006**, *74* (15), 155415−155426.
(21) Seneor, P.; Dlubak, B.; Martin, M.-B.; Anane, A.; Jaffres, H.; Fert, A. Spintronics with Graphene. *MRS Bull.* **2012**, *37* (12), 1245−1254.

(22) Cobas, E.; Friedman, A. L.; van't Erve, O. M. J.; Robinson, J. T.; Jonker, B. T. Graphene As a Tunnel Barrier: Graphene-Based Magnetic Tunnel Junctions. *Nano Lett.* **2012**, *12* (6), 3000−3004.
(23) Iqbal, M. Z.; Iqbal, M. W.; Lee, J. H.; Kim, Y. S.; Chun, S.-H.; Eom, J. Spin Valve Effect of NiFe/Graphene/NiFe Junctions. *Nano Research* **2013**, *6* (5), 373−380.
(24) Chen, J.-J.; Meng, J.; Zhou, Y.-B.; Wu, H.-C.; Bie, Y.-Q.; Liao, Z.-M.; Yu, D.-P. Layer-by-Layer Assembly of Vertically Conducting Graphene Devices. *Nat. Commun.* **2013**, *4*, 1921.
(25) Singh, A. K.; Eom, J. Negative Magnetoresistance in a Vertical Single-Layer Graphene Spin Valve at Room Temperature. *ACS Appl. Mater. Interfaces* **2014**, *6* (4), 2493−2496.
(26) Karpan, V.; Giovannetti, G.; Khomyakov, P.; Talanana, M.; Starikov, A.; Zwierzycki, M.; van den Brink, J.; Brocks, G.; Kelly, P. Graphite and Graphene as Perfect Spin Filters. *Phys. Rev. Lett.* **2007**, *99* (17), 176602.
(27) Weser, M.; Rehder, Y.; Horn, K.; Sicot, M.; Fonin, M.; Preobrajenski, A. B.; Voloshina, E. N.; Goering, E.; Dedkov, Y. S. Induced Magnetism of Carbon Atoms at the Graphene/Ni(111) Interface. *Appl. Phys. Lett.* **2010**, *96* (1), 012504.
(28) Dlubak, B.; Martin, M.-B.; Weatherup, R. S.; Yang, H.; Deranlot, C.; Blume, R.; Schloegl, R.; Fert, A.; Anane, A.; Hofmann, S.; Seneor, P.; Robertson, J. Graphene-Passivated Nickel as an Oxidation-Resistant Electrode for Spintronics. *ACS Nano* **2012**, *6* (12), 10930.
(29) Cobas, E. D.; van 't Erve, O. M. J.; Cheng, S.-F.; Culbertson, J. C.; Jernigan, G. G.; Bussman, K.; Jonker, B. T. Room-Temperature Spin Filtering in Metallic Ferromagnet−Multilayer Graphene−Ferromagnet Junctions. *ACS Nano* **2016**, *10* (11), 10357−10365.
(30) Piquemal-Banci, M.; Galceran, R.; Dubois, S. M.-M.; Zatko, V.; Galbiati, M.; Godel, F.; Martin, M.-B.; Weatherup, R. S.; Petroff, F.; Fert, A.; Charlier, J.-C.; Robertson, J.; Hofmann, S.; Dlubak, B.; Seneor, P. Spin Filtering by Proximity Effects at Hybridized Interfaces in Spin-Valves with 2D Graphene Barriers. *Nat. Commun.* **2020**, *11* (1), 5670.
(31) Shikin, A. M.; Rybkina, A. A.; Rybkin, A. G.; Klimovskikh, I. I.; Skirdkov, P. N.; Zvezdin, K. A.; Zvezdin, A. K. Spin Current Formation at the Graphene/Pt Interface for Magnetization Manipulation in Magnetic Nanodots. *Appl. Phys. Lett.* **2014**, *105* (4), 042407.
(32) Yang, H.; Vu, A. D.; Hallal, A.; Rougemaille, N.; Coraux, J.; Chen, G.; Schmid, A. K.; Chshiev, M. Anatomy and Giant Enhancement of the Perpendicular Magnetic Anisotropy of Cobalt−Graphene Heterostructures. *Nano Lett.* **2016**, *16* (1), 145−151.
(33) Yang, H.; Chen, G.; Cotta, A. A. C.; N'DIaye, A. T.; Nikolaev, S. A.; Soares, E. A.; MacEdo, W. A. A.; Liu, K.; Schmid, A. K.; Fert, A.; Chshiev, M. Significant Dzyaloshinskii-Moriya Interaction at Graphene-Ferromagnet Interfaces Due to the Rashba Effect. *Nat. Mater.* **2018**, *17* (7), 605−609.
(34) Lv, W.; Jia, Z.; Wang, B.; Lu, Y.; Luo, X.; Zhang, B.; Zeng, Z.; Liu, Z. Electric-Field Control of Spin-Orbit Torques in WS_2/Permalloy Bilayers. *ACS Appl. Mater. Interfaces* **2018**, *10* (3), 2843−2849.
(35) Hallal, A.; Liang, J.; Ibrahim, F.; Yang, H.; Fert, A.; Chshiev, M. Rashba-Type Dzyaloshinskii−Moriya Interaction, Perpendicular Magnetic Anisotropy, and Skyrmion States at 2D Materials/Co Interfaces. *Nano Lett.* **2021**, *21* (17), 7138−7144.
(36) Naganuma, H.; Zatko, V.; Galbiati, M.; Godel, F.; Sander, A.; Carrétéro, C.; Bezencenet, O.; Reyren, N.; Martin, M.-B.; Dlubak, B.; Seneor, P. A Perpendicular Graphene/Ferromagnet Electrode for Spintronics. *Appl. Phys. Lett.* **2020**, *116* (17), 173101.
(37) Galbiati, M.; Delprat, S.; Mattera, M.; Mañas-Valero, S.; Forment-Aliaga, A.; Tatay, S.; Deranlot, C.; Seneor, P.; Mattana, R.; Petroff, F. Recovering Ferromagnetic Metal Surfaces to Fully Exploit Chemistry in Molecular Spintronics. *AIP Advances* **2015**, *5* (5), 057131.
(38) Weatherup, R. S.; Dlubak, B.; Hofmann, S. Kinetic Control of Catalytic CVD for High-Quality Graphene at Low Temperatures. *ACS Nano* **2012**, *6* (11), 9996−10003.
(39) Martin, M.-B.; Dlubak, B.; Weatherup, R. S.; Piquemal-Banci, M.; Yang, H.; Blume, R.; Schloegl, R.; Collin, S.; Petroff, F.; Hofmann, S.; Robertson, J.; Anane, A.; Fert, A.; Seneor, P. Protecting Nickel with Graphene Spin-Filtering Membranes: A Single Layer Is Enough. *Appl. Phys. Lett.* **2015**, *107* (1), 012408.
(40) Martin, M.-B.; Dlubak, B.; Weatherup, R. S.; Yang, H.; Deranlot, C.; Bouzehouane, K.; Petroff, F.; Anane, A.; Hofmann, S.; Robertson, J.; Fert, A.; Seneor, P. Sub-Nanometer Atomic Layer Deposition for Spintronics in Magnetic Tunnel Junctions Based on Graphene Spin-Filtering Membranes. *ACS Nano* **2014**, *8* (8), 7890.
(41) Weatherup, R. S.; Bayer, B. C.; Blume, R.; Baehtz, C.; Kidambi, P. R.; Fouquet, M.; Wirth, C. T.; Schlögl, R.; Hofmann, S. On the Mechanisms of Ni-Catalysed Graphene Chemical Vapour Deposition. *ChemPhysChem* **2012**, *13* (10), 2544−2549.
(42) Weatherup, R. S.; Amara, H.; Blume, R.; Dlubak, B.; Bayer, B. C.; Diarra, M.; Bahri, M.; Cabrero-Vilatela, A.; Caneva, S.; Kidambi, P. R.; Martin, M.-B.; Deranlot, C.; Seneor, P.; Schloegl, R.; Ducastelle, F.; Bichara, C.; Hofmann, S. Interdependency of Subsurface Carbon Distribution and Graphene−Catalyst Interaction. *J. Am. Chem. Soc.* **2014**, *136* (39), 13698−13708.
(43) Patera, L. L.; Africh, C.; Weatherup, R. S.; Blume, R.; Bhardwaj, S.; Castellarin-Cudia, C.; Knop-Gericke, A.; Schloegl, R.; Comelli, G.; Hofmann, S.; Cepek, C. In Situ Observations of the Atomistic Mechanisms of Ni Catalyzed Low Temperature Graphene Growth. *ACS Nano* **2013**, *7* (9), 7901−7912.
(44) Ferrari, A. C.; Basko, D. M. Raman Spectroscopy as a Versatile Tool for Studying the Properties of Graphene. *Nat. Nanotechnol.* **2013**, *8* (4), 235−246.
(45) Grosvenor, A. P.; Biesinger, M. C.; Smart, R. St. C.; McIntyre, N. S. New Interpretations of XPS Spectra of Nickel Metal and Oxides. *Surf. Sci.* **2006**, *600* (9), 1771−1779.
(46) Bouzehouane, K.; Fusil, S.; Bibes, M.; Carrey, J.; Blon, T.; le Dû, M.; Seneor, P.; Cros, V.; Vila, L. Nanolithography Based on Real-Time Electrically Controlled Indentation with an Atomic Force Microscope for Nanocontact Elaboration. *Nano Lett.* **2003**, *3* (11), 1599−1602.
(47) Zhang, Y.; Brar, V. W.; Wang, F.; Girit, C.; Yayon, Y.; Panlasigui, M.; Zettl, A.; Crommie, M. F. Giant Phonon-Induced Conductance in Scanning Tunnelling Spectroscopy of Gate-Tunable Graphene. *Nat. Phys.* **2008**, *4* (8), 627−630.
(48) Dedkov, Y. S.; Fonin, M. Electronic and Magnetic Properties of the Graphene−Ferromagnet Interface. *New J. Phys.* **2010**, *12* (12), 125004.
(49) de Teresa, J. M.; Barthélémy, A.; Fert, A.; Contour, J. P.; Montaigne, F.; Seneor, P. Role of Metal-Oxide Interface in Determining the Spin Polarization of Magnetic Tunnel Junctions. *Science (1979)* **1999**, *286* (5439), 507−509.
(50) Moodera, J. S.; Mathon, G. Spin Polarized Tunneling in Ferromagnetic Junctions. *J. Magn. Magn. Mater.* **1999**, *200*, 248−273.
(51) Tsymbal, E. Y.; Mryasov, O. N.; LeClair, P. R. Spin-Dependent Tunnelling in Magnetic Tunnel Junctions. *J. Phys.: Condens. Matter* **2003**, *15* (4), R109−R142.
(52) Zhang, S.; Levy, P. M.; Marley, A. C.; Parkin, S. S. P. Quenching of Magnetoresistance by Hot Electrons in Magnetic Tunnel Junctions. *Phys. Rev. Lett.* **1997**, *79* (19), 3744.
(53) Bratkovsky, A. M. Assisted Tunneling in Ferromagnetic Junctions and Half-Metallic Oxides. *Appl. Phys. Lett.* **1998**, *72* (18), 2334.
(54) Karpan, V. M.; Khomyakov, P. A.; Starikov, A. A.; Giovannetti, G.; Zwierzycki, M.; Talanana, M.; Brocks, G.; Van Den Brink, J.; Kelly, P. J. Theoretical Prediction of Perfect Spin Filtering at Interfaces between Close-Packed Surfaces of Ni or Co and Graphite or Graphene. *Physical Review B - Condensed Matter and Materials Physics* **2008**, *78* (19), 195419.
(55) Yazyev, O. V.; Pasquarello, A. Magnetoresistive Junctions Based on Epitaxial Graphene and Hexagonal Boron Nitride. *Physical Review B - Condensed Matter and Materials Physics* **2009**, *80* (3), 035408.
(56) Asshoff, P. U.; Sambricio, J. L.; Rooney, A. P.; Slizovskiy, S.; Mishchenko, A.; Rakowski, A. M.; Hill, E. W.; Geim, A. K.; Haigh, S.

https://doi.org/10.1021/acsnano.2c03625
ACS Nano 2022, 16, 14007−14016

J.; Fal'Ko, V. I.; Vera-Marun, I. J.; Grigorieva, I. v. Magnetoresistance of Vertical Co-Graphene-NiFe Junctions Controlled by Charge Transfer and Proximity-Induced Spin Splitting in Graphene. *2D Materials* **2017**, *4* (3), 031004.
(57) Paulsson, M.; Brandbyge, M. Transmission Eigenchannels from Nonequilibrium Green's Functions. *Physical Review B - Condensed Matter and Materials Physics* **2007**, *76* (11), 115117.
(58) Žutić, I.; Matos-Abiague, A.; Scharf, B.; Dery, H.; Belashchenko, K. Proximitized Materials. *Mater. Today* **2019**, *22*, 85−107.
(59) Galbiati, M.; Tatay, S.; Barraud, C.; Dediu, A. V.; Petroff, F.; Mattana, R.; Seneor, P. Spinterface: Crafting Spintronics at the Molecular Scale. *MRS Bull.* **2014**, *39* (07), 602−607.
(60) Piquemal-Banci, M.; Galceran, R.; Godel, F.; Caneva, S.; Martin, M.-B.; Weatherup, R. S.; Kidambi, P. R.; Bouzehouane, K.; Xavier, S.; Anane, A.; Petroff, F.; Fert, A.; Dubois, S. M.-M.; Charlier, J.-C.; Robertson, J.; Hofmann, S.; Dlubak, B.; Seneor, P. Insulator-to-Metallic Spin-Filtering in 2D-Magnetic Tunnel Junctions Based on Hexagonal Boron Nitride. *ACS Nano* **2018**, *12* (5), 4712−4718.
(61) Zatko, V.; Galbiati, M.; Dubois, S. M.-M.; Och, M.; Palczynski, P.; Mattevi, C.; Brus, P.; Bezencenet, O.; Martin, M.-B.; Servet, B.; Charlier, J.-C.; Godel, F.; Vecchiola, A.; Bouzehouane, K.; Collin, S.; Petroff, F.; Dlubak, B.; Seneor, P. Band-Structure Spin-Filtering in Vertical Spin Valves Based on Chemical Vapor Deposited WS_2. *ACS Nano* **2019**, *13* (12), 14468−14476.
(62) Naganuma, H.; Nishijima, M.; Adachi, H.; Uemoto, M.; Shinya, H.; Yasui, S.; Morioka, H.; Hirata, A.; Godel, F.; Martin, M.-B.; Dlubak, B.; Seneor, P.; Amemiya, K. Unveiling a Chemisorbed Crystallographically Heterogeneous Graphene/ $L1_0$ -FePd Interface with a Robust and Perpendicular Orbital Moment. *ACS Nano* **2022**, *16* (3), 4139−4151.
(63) Dion, M.; Rydberg, H.; Schröder, E.; Langreth, D. C.; Lundqvist, B. I. Van Der Waals Density Functional for General Geometries. *Phys. Rev. Lett.* **2004**, *92* (24), 246401.
(64) Klimeš, J.; Bowler, D. R.; Michaelides, A. Chemical Accuracy for the van Der Waals Density Functional. *J. Phys.: Condens. Matter* **2009**, *22* (2), 022201.
(65) Soler, J. M.; Artacho, E.; Gale, J. D.; García, A.; Junquera, J.; Ordejón, P.; Sánchez-Portal, D. The SIESTA Method for Ab Initio Order-N Simulation. *J. Phys.: Condens. Matter* **2002**, *14* (11), 2745.
(66) Brandbyge, M.; Mozos, J. L.; Ordejón, P.; Taylor, J.; Stokbro, K. Density-Functional Method for Nonequilibrium Electron Transport. *Phys. Rev. B* **2002**, *65* (16), 165401.
(67) Papior, N.; Lorente, N.; Frederiksen, T.; García, A.; Brandbyge, M. Improvements on Non-Equilibrium and Transport Green Function Techniques: The next-Generation Transiesta. *Comput. Phys. Commun.* **2017**, *212*, 8−24.
(68) Lopez Sancho, M. P.; Lopez Sancho, J. M.; Rubio, J. Highly Convergent Schemes for the Calculation of Bulk and Surface Green Functions. *Journal of Physics F: Metal Physics* **1985**, *15* (4), 851.
(69) Sanvito, S.; Rocha, A. R. Molecular-Spintronics: The Art of Driving Spin Through Molecules. *J. Comput. Theor. Nanosci.* **2006**, *3* (5), 624−642.
(70) Huertas-Hernando, D.; Guinea, F.; Brataas, A. Spin-Orbit Coupling in Curved Graphene, Fullerenes, Nanotubes, and Nanotube Caps. *Phys. Rev. B* **2006**, *74* (15), 155426.
(71) Krinichnyi, V.; Chemerisov, S.; Lebedev, Y. S. EPR and Charge-Transport Studies of Polyaniline. *Phys. Rev. B* **1997**, *55* (24), 16233.
(72) Shim, J. H.; Raman, K. v.; Park, Y. J.; Santos, T. S.; Miao, G. X.; Satpati, B.; Moodera, J. S. Large Spin Diffusion Length in an Amorphous Organic Semiconductor. *Phys. Rev. Lett.* **2008**, *100* (22), 226603.

https://doi.org/10.1021/acsnano.2c03625
ACS Nano 2022, 16, 14007−14016